Standing Waves Induced by Valley-Mismatched Domains in Ferroelectric SnTe Monolayers

Kai Chang, Brandon J. Miller, Hao Yang, Haicheng Lin, Stuart S. P. Parkin, Salvador Barraza-Lopez, Qi-Kun Xue, Xi Chen, and Shuai-Hua Ji

Phys. Rev. Lett. **122**, 206402 — Published 24 May 2019

DOI: 10.1103/PhysRevLett.122.206402

Standing waves induced by valley mismatched domains in ferroelectric SnTe monolayers

Kai Chang,[1,2,4] Brandon J. Miller,[3] Hao Yang,[2] Haicheng Lin,[1,4] Stuart S. P. Parkin,[2,*] Salvador Barraza-Lopez,[3] Qi-Kun Xue,[1,4] Xi Chen,[1,4,†] and Shuai-Hua Ji[1,4,5,‡]

[1] *State Key Laboratory of Low-Dimensional Quantum Physics, Department of Physics, Tsinghua University, Beijing 100084, China*
[2] *Max-Planck Institute of Microstructure Physics, Weinberg 2, 06120 Halle (Saale), Germany*
[3] *Department of Physics, University of Arkansas, Fayetteville, Arkansas 72701, USA*
[4] *Collaborative Innovation Center of Quantum Matter, Beijing 100084, China*
[5] *RIKEN Center for Emergent Matter Science (CEMS) - Wako, Saitama 351-0198, Japan*

(Dated: April 1, 2019)

Two-dimensional (2D) quasiparticle standing waves originate from the interference of coherent quantum states, and are usually created by the scattering off edges, atomic steps or adatoms that induce large potential barriers. We report standing waves close to the valence band maximum (E_V), confined by electrically neutral domain walls of newly discovered ferroelectric SnTe monolayers, as revealed by spatially resolved scanning tunneling spectroscopy. *Ab initio* calculations show that this novel confinement arises from the polarization lifted hole valley degeneracy and a $\sim 90^\circ$ rotation of the Brillouin zones that renders holes' momentum mismatched across neighboring domains. These results show a potential for polarization-tuned valleytronics in 2D ferroelectrics.

Standing waves are created by the superposition of phase coherent waves of identical frequency, and are common in mechanical and optical settings. Electron or hole (quasiparticle) standing waves can be probed with scanning tunneling microscopes (STM) that provide atomic resolution of material surfaces. Quasiparticle standing waves induced by scattering from atomic steps were first observed on noble metal surfaces [1–3] and the confinement of surface states by two parallel atomic steps was explained with a Fabry-Pérot resonator model [4, 5]. Furthermore, arranging adatoms into quantum corral shapes on atomically flat metal surfaces, quantum mirage patterns have been created [6–8]. These confined surface states are free-like quasiparticles with parabolic band dispersion centered at the $\Gamma-$point of the Brillouin zone [4–8] that are scattered by potential barriers at structural defects [9]. Here, we report a mechanism to induce quasiparticle standing waves that does not require large potential barriers, but mismatched valleys at neighboring domains of a 2D ferroelectric.

2D ferroelectrics are a unique platform to study the interplay among electronic structure and ferroelectricity. It is challenging to probe the electronic states of bulk ferroelectrics by STM due to their insulating nature. As the thickness of a ferroelectric film reaches a few atomic layers, a detectable tunneling current could be obtained by STM as long as the substrate is metallic. Although topography and differential conductance ($\mathrm{d}I/\mathrm{d}V$) spectral maps of ferroelectric films have been documented [13–17], STM studies of quasiparticle standing waves remain difficult due to the need for ultra clean and uniform surfaces. 2D ferroelectrics with a van der Waals, layered atomic structure ensure atomically clean surfaces [18–25] and make their electronic structures accessible by STM. Among them, SnTe monolayers (SnTe MLs) are especially interesting because of their regular 90° head-to-tail domains with in-plane polarizations [18, 19] and the two-valley electronic band structure near its valence band maximum E_V [26–28], which will be shown to give rise to standing waves.

Our experiments were carried out in a combined molecular beam epitaxy and STM system in ultra-high vacuum. An n-doped, Si-terminated 6H-SiC(0001) substrate was heated by passing a direct current through it, and temperature was monitored with an infrared pyrometer. After a sequential high temperature annealing up to 1400° C with a base pressure lower than 2×10^{-10} Torr, uniform epitaxial graphene layers were formed [18]. Then, SnTe nanoplates were grown on epitaxial graphene by evaporating SnTe molecules from an hBN crucible (SnTe granules from Alfa Aesar, 99.999%, kept at 450° C) onto substrates at 150∼200°C. SnTe nanoplates with lateral sizes up to 1 μm and atomic defect densities lower than 10^{10} cm^{-3} were obtained. SnTe MLs were found among those nanoplates. *In situ* experimental data were acquired at 4.7 K with Pt/Ir alloy tips in a low-temperature STM connected to the growth chamber. A sinusoidal modulation voltage $V_{\mathrm{mod}} = 0.01$ V with a frequency of 913 Hz was added to the sample bias voltage V_s during scanning tunneling spectroscopy (STS) measurements.

Ab initio calculations with the *SIESTA* code [29] that include spin-orbit coupling [30] help relate the standing wave pattern to the electronic structure of the SnTe ML. They utilized norm-conserving Troullier-Martins pseudopotentials [31, 32] with van der Waals corrections [33, 34]. The real-space grid in which the Poisson equation is solved had a 300 Ry energy cutoff. Standard (DZP) basis sets [35] with a 0.03 eV energy shift and a Monkhorst-Pack [36] mesh of $18 \times 18 \times 1$ $k-$points were

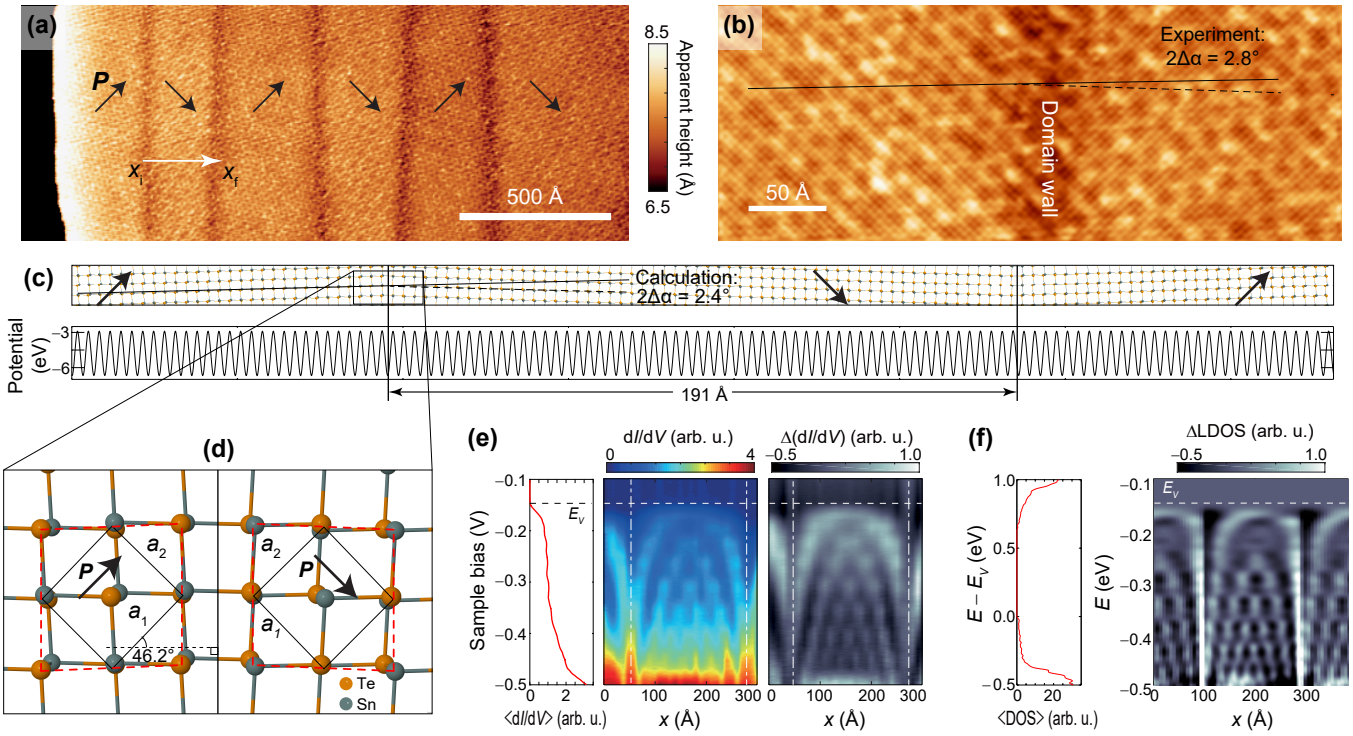

FIG. 1. (a) STM topography of a SnTe monolayer. Imaging conditions: sample bias voltage $V_s = -0.2$ V, tunneling current $I_t = 20$ pA. (b) Atom resolved STM topography across two neighboring domains. The solid and dashed lines indicate one lattice direction of the rhombic cells in neighboring domains. There is a mismach angle $2\Delta\alpha = 2.8°$ among those two directions. Here, $V_s = -0.2$ V and $I_t = 100$ pA. (c) Relaxed domain structure from *ab initio* calculations; $2\Delta\alpha = 2.4°$ there. The electrostatic potential is shown in the lower subplot. (d) Zoom-in of the domain wall. Solid and dashed lines indicate the rectangular and rhombic cells, respectively. (e) $\mathrm{d}I/\mathrm{d}V$ spectra across the horizontal white arrow in (a): average $\langle \frac{dI}{dV} \rangle = \frac{1}{x_f - x_i} \int_{x_i}^{x_f} \frac{dI}{dV}(x) dx$ (left), spatially resolved $\mathrm{d}I/\mathrm{d}V$ (center), and the same spectra with a polynomial background subtracted (right). $V_s = -0.5$ V, $I_t = 100$ pA. Vertical dashed lines indicate the positions of domain walls. (f) Calculated average density of states $\langle \mathrm{LDOS} \rangle$ (left) and $\Delta\mathrm{LDOS} = \mathrm{LDOS}(x) - \langle \mathrm{LDOS} \rangle$ (right) of the structure shown in (b). E_V was shifted to match experiment.

employed. The vertical vacuum among periodic slabs was set to 20 Å, and structural optimizations were performed with a force tolerance of 10^{-3} eV/Å [19].

Ferroelectricity is coupled to the electronic band structure of SnTe MLs. Below the transition temperature of 270 K [18], the emerging in-plane spontaneous polarization **P** breaks the inversion symmetry of the ML, turning its space group into $Pmn2_1$ on a structure isomorphic to that of GeS, GeSe, SnS and SnSe MLs [19]. **P** introduces an effective electric field which in turn induces a momentum-dependent effective magnetic field via spin-orbit coupling, which splits the sub-bands with orthogonal spin components. It also lifts the valley degeneracy and reduces the number of hole valleys from four to two [37], which will be crucial for quasiparticle confinement in between parallel domains.

Band bending in 2D ferroelectrics induced by bound charges can be directly imaged by STM. Fig. 1(a) is an STM topography image of the SnTe ML: when scanning with a negative bias voltage, the flake shows a larger apparent height at the far-left edge, implying a negative bound charge and an upward band bending; methods for measuring band bending at edges have been reported before [18, 19]. At each domain, **P** was determined from (i) the direction of lattice distortion and (ii) the directions of band bending at the edges [18]. Straight 90° domain walls appear darker, and **P** is indicated by arrows (↗ or ↘) joining head to tail. (The apparent height of the domain walls is lower because the nodes of electronic standing waves locate there, as described later.) Fig. 1(b) is the atomically resolved STM topography of two neighboring domains, in which the lattice distortion is exhibited by $\Delta\alpha = \pi/2 - \alpha$, with α the rhombic angle of a distorted rocksalt unit cell. The lattice is continuous at the domain wall, with no atomic defects at the interface. A hexagonal pattern observed on the topographic image (Fig. 1(b)) is induced by the 6×6 superstructure of the graphene/SiC substrate.

Fig. 1(c) shows the relaxed atomic structure of a periodic supercell with two consecutive 191 Å wide domains, as obtained from *ab initio* calculations. The left (right) domain was built by rotating the rectangular unit cell

by 46.2° (−46.2°) with respect to the horizontal, so that the rhombic cells shown in red dashed lines have two sides oriented parallel to the domain walls. $\Delta\alpha = 1.2°$ in Fig. 1(c) is only 0.2° smaller than its magnitude in experiment (Fig. 1(b)) thanks to the inclusion of van der Waals corrections. The electrostatic potential in Fig. 1(c) has a negligible build-up (smaller than 0.04 V) near domain walls: it is nearly flat, beyond the standard atomic scale oscillations. Domain walls lack significant bound charges because $\nabla \cdot \mathbf{P}$ is nearly zero on them, which means that the polarization component perpendicular to domain walls is almost constant. A zoom-in of the electrostatic potential around the domain wall is provided as Supplementary Material [38]. Fig. 1(d) is a zoom-in of the domain wall in which polarization vectors meet at a $2 \times 46.2 = 92.4°$ angle. Using conventional ferroelectrics language, we labeled these as 90° domains.

The experimental spatially resolved $\mathrm{d}I/\mathrm{d}V$ spectra acquired along the white horizontal arrow in Fig. 1(a) exhibits a standing wave pattern along a 235 Å width between domain walls, for energies below E_V (located at −0.15 eV) [Fig. 1(e)]. As the energy decreases, the number of nodes of the standing wave pattern increases and the oscillation period length becomes shorter. The resulting pattern is reminiscent of a particle-in-a-box, hole-like energy dispersion. The calculated local density of states (LDOS) of the supercell structure in Fig. 1(f) reproduces the standing wave pattern. Taken together, Figs. 1(c), (e) and (f) indicate that standing waves exist despite of the absence of a potential energy barrier at domain walls. This phenomena originates from mismatched electronic structures across domains, as discussed below.

The electronic band structure of a SnTe ML shown in Fig. 2(b) was obtained along the high symmetry path displayed in Fig. 2(a). The identical band gap in the spatially averaged LDOS over periodic domains [Fig. 1(f), left panel] and the band structure calculated on a unit cell [Fig. 2(b)] indicates that the domain walls create no additional quasiparticle states within the band gap. Calculated constant energy contours (CECs) below E_V are shown in Fig. 2(c). As the crystalline symmetry is lowered below the ferroelectric transition temperature, the four-fold valley degeneracy is lifted, and the spontaneous polarization pushes the two hole valleys located along the $\Gamma - Y$ line to energies ∼0.3 eV below the valence band edges, located along the $\Gamma - X$ line, leaving only two valleys for energies in a 0.3 eV energy range below E_V.

Given that there is nearly no potential energy build-up at the 90° domain walls (Fig. 1(c)), standing waves originate from a finite domain wall reflection probability induced by the mismatch of valley crystal momenta at consecutive domain walls; see Fig. 2(d). As valleys become rotated at opposite sides of a domain wall, a quasiparticle traveling from the left domain cannot proceed to the one to the right, unless its crystal momentum $\mathbf{k}$ experiences a change $q = |\mathbf{q}| \sim 0.8$ Å^{-1} shown by red dashed arrows in

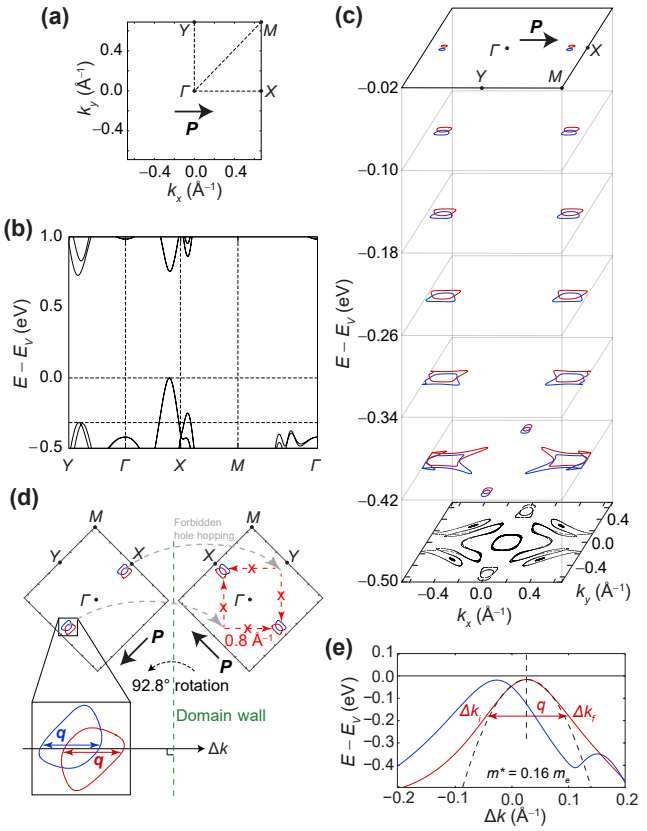

FIG. 2. (a) First Brillouin zone and (b) band structure of SnTe ML. (c) Constant energy contours (CECs) for energies below E_V. Red and blue represent orthogonal spin polarizations. (d) Momentum mismatch across domain walls prohibits hole transmission across domains. The intra-band scattering vectors $\mathbf{q}$ are labeled in one valley. (e) An $E(\mathbf{k})$ cut along a line across the center of a valley and perpendicular to the domain wall. Δk is the distance away from the valley center. A quadratic fit yields $m^* = 0.162 m_e$ along this direction.

the Figure, which is longer than half of the Brillouin zone width. The probability of such processes is low because mechanisms that can assist transmission, such as long-$\mathbf{q}$ phonons, are rare at liquid helium temperature. Instead, quasiparticles have a higher probability to be reflected off domain walls, by means of short-$\mathbf{q}$ scattering processes within a single valley.

The allowed wavelengths of standing waves are determined by the CECs' shapes, which are in turn influenced by spin-orbit coupling. Allowed scattering vectors $\mathbf{q}$ must link two states with the same spin polarization on the CECs, and be perpendicular to the domain wall. Fig. 2(d) shows CECs at an energy of $E_V - 0.18$ eV. Fig. 2(e) is an $E(\Delta\mathbf{k})$ cut of a hole valley on the left domain in Fig. 2(d), along the direction perpendicular to the domain wall, in which a Rashba splitting is revealed. A quadratic fitting yields an effective mass $m^* = 0.162 m_e$ near E_V at this specific orientation.

Figure 3(a) is the standing wave pattern in a wider

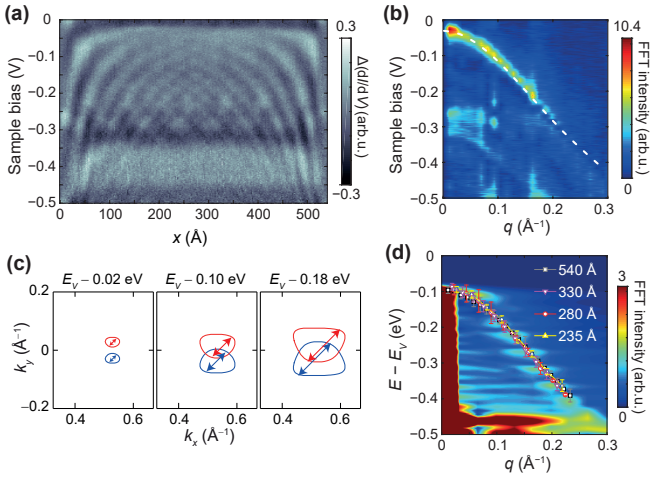

FIG. 3. (a) Spatially resolved $\Delta \mathrm{d}I/\mathrm{d}V(x)$ across a 540 Å wide domain. $V_s = -0.5$ V, $I_t = 100$ pA. (b) The Fourier transform of (a) is the energy dispersion of scattering vectors, $E(q)$. The dashed white curve was obtained from the $E(k)$ dispersion of the band colored in red in Fig. 2(e). (c) Scattering vectors extracted from experiments, overlaid onto calculated CECs. (d) Fourier transform of the ΔLDOS shown in Fig. 1(f). The $E(q)$ extracted from the experimental $\mathrm{d}I/\mathrm{d}V$ data of domains with increasing widths are superimposed.

domain ($L = 540$ Å). The energy dispersion of $q = |\mathbf{q}|$ is its Fourier transform at each bias voltage, and shown in Fig. 3(b). The dashed white curve overlaid onto the Fourier transform is the $E(\mathbf{q})$ dispersion obtained by relating the initial and final states of the $E(\Delta k)$ line cut in Fig. 2(e) as $q(E) = \Delta k_f(E) - \Delta k_i(E)$. We also compared the values of q obtained from experiments –which provide a window into the electronic structure– with those joining opposite ends of the CECs at three increasing energies in Fig. 3(c). The $E(\mathbf{q})$ dispersion extracted from several domains with different widths –obtained from a direct count of standing wave nodes at a given bias voltage $n(V_s)$ using the expression $q(V_s) = 2\pi[n(V_s) + 1]/L$ (see Ref. [38] for additional details)– continue to agree with the Fourier transform of the calculated ΔLDOS in Fig. 1(f). The agreement between experiment and theory implies that scattering occurs within a single spin polarized band and that spin-flipping is forbidden. Recalling the long spin diffusion lengths in high-quality semiconductors and semimetals, for example, 235 nm at 12 K in MoS_2 [39] and 2.4 μm at 300 K in graphene [40], it is reasonable that spin-conserved reflections are dominating in between the domain walls separated by several tens of nm in monolayer SnTe.

In addition to the strong $E(\mathbf{q})$ dispersion resolved close to VBM in Figure 2(b), another weaker hole-like dispersion with its apex at −0.32 eV can also be seen. The weaker dispersion can be ascribed to the intra-valley scattering in the emerging bands along $\Gamma - Y$ direction, as Figure 1(b) shows.

Now we turn to the discussion of the reflection and transmission probabilities at the domain walls of monolayer SnTe. Quasiparticle standing waves of topological surface states with a Dirac band dispersion arise from the scattering off atomic steps as well [10–12]. But different from the trivial surface states on noble metals, these time-reversal symmetry protected topological surface states show non-negligible transmission through atomic steps [12]. Compared to these two previous physical scenarios, the electronic states near the VBM of SnTe ML shows high reflection probability, even though no significant potential barrier exists at the domain walls.

Analysis of the reflection probability of electronic states from the domain walls is accomplished semi-quantitatively using the 235 Å domain in Fig. 1(e). We employ a Fabry-Pérot resonator integral [4] to simulate the standing wave pattern and estimate the reflection probability $|r|^2$ [38]. Lack of spin-flips permits using a spin-independent model. Phase shifts upon reflection were set to $-\pi$ at both walls. Comparing the simulated standing wave profiles and the experiments, a reflection amplitude $|r| = 0.7 \pm 0.1$ is obtained, which is comparable to that estimated at atomic steps on Ag(111) surfaces [4].

We searched for evidence of transmission at domain walls, by checking quasi-continuous standing wave patterns in a wide domain ($L > 1000$ Å) neighboring a narrow domain ($L = 64$ Å) [38], similar to the method used to reveal the transmission through atomic steps of topological surface states [12]. When finite transmission probability exists, the oscillation amplitude of the standing waves in the wide domain is suppressed at energies corresponding to the discrete standing wave levels in the narrow domain. Such suppression is not observed in our experiments, implying a low transmission probability that is beyond the resolution of our instruments. We note that the reflection probability of domains is not 100%. The remaining amplitude is probably scattered into the metallic substrate, similar to the situation occurring in Refs. [1, 4, 12].

Angle-resolved photoemission spectroscopy (ARPES) measurements are usually performed on macroscopic samples. For this material, ARPES spectra would likely include information from many domains (i.e., from misaligned valleys). Due to its atomic resolution, STM is an ideal experimental probe of the electronic valley structure for this 2D ferroelectric material family; and the quasiparticle confinement in these domains hereby documented can lead to new mechanisms for spontaneous-polarization-tuned devices.

In conclusion, electronic standing wave patterns below the valence band maximum induced by electrically neutral 90° domain walls were discovered in ferroelectric SnTe MLs by low-temperature scanning tunneling microscopy experiments and *ab initio* calculations, despite of the absence of a significant potential barrier at domain

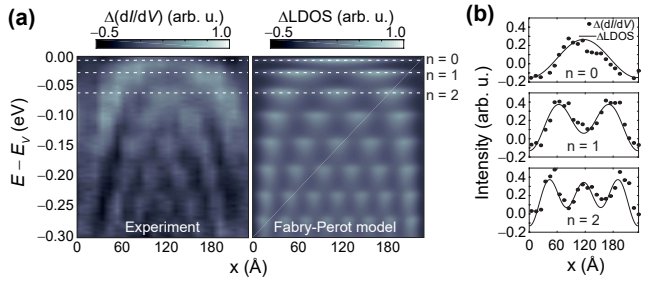

FIG. 4. (a) Comparing the experimental standing wave pattern of the 235 Å wide domain with the result from a Fabry-Pérot model. (b) Constant energy cuts from both the experimental and calculated data for the first three standing wave levels ($n = 0, 1, 2$) at energies shown by dashed lines in (a).

walls. Confinement is ascribed to the mismatch of crystal momenta across consecutive domains. This phenomenology could be helpful for the development of valleytronic devices that are tuned by the spontaneous polarization of domains in 2D ferroelectrics.

K.C., H.L., Q.-K.X., X.C. and S.-H.J. were supported by the National Natural Science Foundation of China (Grants 51561145005, 11574175 and 11622433) and the Ministry of Science and Technology of China (Grants 2016YFA0301002 and 2018YFA0305603). K.C., H.Y. and S.S.P.P. were funded by the Deutsche Forschungsgemeinschaft, Project PA 1812/2-1. S.B.L. was supported by the U.S. Department of Energy, Basic Energy Sciences, Early Career Award DE-SC0016139. Calculations were done at *Trestles*, funded by the National Science Foundation and the Arkansas Economic Development Commission, and the U of A Office of the Vice Provost for Research and Innovation.

* stuart.parkin@mpi-halle.mpg.de
† xc@mail.tsinghua.edu.cn
‡ shji@mail.tsinghua.edu.cn

[1] M. F. Crommie, C. P. Lutz, and D. M. Eigler, Nature **363**, 524 (1993).
[2] Y. Hasegawa and P. Avouris, Phys. Rev. Lett. **71**, 1071 (1993).
[3] P. Avouris and I.-W. Lyo, Science **264**, 942 (1994).
[4] L. Bürgi, O. Jeandupeux, A. Hirstein, H. Brune, and K. Kern, Phys. Rev. Lett. **81**, 5370 (1998).
[5] L. Bürgi, O. Jeandupeux, H. Brune, and K. Kern, Phys. Rev. Lett. **82**, 4516 (1999).
[6] M. F. Crommie, C. P. Lutz, and D. M. Eigler, Science **262**, 218 (1993).
[7] H. C. Manoharan, C. P. Lutz, and D. M. Eigler, Nature **403**, 512 (2000).
[8] G. A. Fiete and E. J. Heller, Rev. Mod. Phys. **75**, 933 (2003).
[9] J. E. Ortega, J. Lobo-Checa, G. Peschel, S. Schirone, Z. M. Abd El-Fattah, M. Matena, F. Schiller, P. Borghetti, P. Gambardella, and A. Mugarza, Phys. Rev. B **87**, 115425 (2013).
[10] T. Zhang, P. Cheng, X. Chen, J.-F. Jia, X. Ma, K. He, L. Wang, H. Zhang, X. Dai, Z. Fang, X. Xie, and Q.-K. Xue, Phys. Rev. Lett. **103**, 266803 (2009).
[11] J. Wang, W. Li, P. Cheng, C. Song, T. Zhang, P. Deng, X. Chen, X. Ma, K. He, J.-F. Jia, Q.-K. Xue, and B.-F. Zhu, Phys. Rev. B **84**, 235447 (2011).
[12] J. Seo, P. Roushan, H. Beidenkopf, Y. S. Hor, R. J. Cava, and A. Yazdani, Nature **466**, 343 (2010).
[13] B. C. Huang, Y. T. Chen, Y. P. Chiu, Y. C. Huang, J. C. Yang, Y. C. Chen, and Y. H. Chu, Appl. Phys. Lett. **100**, 122903 (2012).
[14] O. Kuffer, I. Maggio-Aprile, J.-M. Triscone, Ø. Fischer, and C. Renner, Appl. Phys. Lett. **77**, 1701 (2000).
[15] A. V. Bune, V. M. Fridkin, S. Ducharme, L. M. Blinov, S. P. Palto, A. V. Sorokin, S. G. Yudin, and A. Zlatkin, Nature **391**, 874 (1998).
[16] H. Qu, W. Yao, T. Garcia, J. Zhang, A. V. Sorokin, S. Ducharme, P. A. Dowben, and V. M. Fridkin, Appl. Phys. Lett. **82**, 4322 (2003).
[17] X. Chen, S. Yang, J.-H. Kim, H.-D. Kim, J.-S. Kim, G. Rojas, R. Skomski, H. Lu, A. Bhattacharya, T. Santos, N. Guisinger, M. Bode, A. Gruverman, and A. Enders, New J. Phys. **13**, 083037 (2011).
[18] K. Chang, J. Liu, H. Lin, N. Wang, K. Zhao, A. Zhang, F. Jin, Y. Zhong, X. Hu, W. Duan, Q. Zhang, L. Fu, Q.-K. Xue, X. Chen, and S.-H. Ji, Science **353**, 274 (2016).
[19] K. Chang, T. Kaloni, H. Lin, A. BedoyaPinto, A. K. Pandeya, I. Kostanovskiy, K. Zhao, Y. Zhong, X. Hu, Q. Xue, X. Chen, S.-H. Ji, S. Barraza-Lopez, and S. S. P. Parkin, Adv. Mater. **31**, 1804428 (2019).
[20] F. Liu, L. You, K. L. Seyler, X. Li, P. Yu, J. Lin, X. Wang, J. Zhou, H. Wang, H. He, S. T. Pantelides, W. Zhou, P. Sharma, X. Xu, P. M. Ajayan, J. Wang, and Z. Liu, Nat. Commun. **7**, 12357 (2016).
[21] Y. Zhou, D. Wu, Y. Zhu, Y. Cho, Q. He, X. Yang, K. Herrera, Z. Chu, Y. Han, M. C. Downer, H. Peng, and K. Lai, Nano Lett. **17**, 5508 (2017).
[22] J. Xiao, H. Zhu, Y. Wang, W. Feng, Y. Hu, A. Dasgupta, Y. Han, Y. Wang, D. A. Muller, L. W. Martin, P.A. Hu, and X. Zhang, Phys. Rev. Lett. **120**, 227601 (2018).
[23] C. Cui, W.-J. Hu, X. Yan, C. Addiego, W. Gao, Y. Wang, Z. Wang, L. Li, Y. Cheng, P. Li, X. Zhang, H. N. Alshareef, T. Wu, W. Zhu, X. Pan, and L.-J. Li, Nano Lett. **18**, 1253 (2018).
[24] C. Zheng, L. Yu, L. Zhu, J. L. Collins, D. Kim, Y. Lou, C. Xu, M. Li, Z. Wei, Y. Zhang, M. T. Edmonds, S. Li, J. Seidel, Y. Zhu, J. Z. Liu, W.-X. Tang, and M. S. Fuhrer, Sci. Adv. **4**, eaar7220 (2018).
[25] Z. Fei, W. Zhao, T. A. Palomaki, B. Sun, M. K. Miller, Z. Zhao, J. Yan, X. Xu, and D. H. Cobden, Nature **560**, 336 (2018).
[26] L. C. Gomes and A. Carvalho, Phys. Rev. B **92**, 085406 (2015).
[27] A. S. Rodin, L. C. Gomes, A. Carvalho, and A. H. Castro Neto, Phys. Rev. B **93**, 045431 (2016).
[28] P. Z. Hanakata, A. Carvalho, D. K. Campbell, and H. S. Park, Phys. Rev. B **94**, 035304 (2016).
[29] J. M. Soler, E. Artacho, J. D. Gale, A. García, J. Junquera, P. Ordejón, and D. Sánchez-Portal, J. Phys.: Condens. Matter **14**, 2745 (2002).
[30] L. Fernández-Seivane, M. A. Oliveira, S. Sanvito, and J. Ferrer, J. Phys.: Condensed Matter **18**, 7999 (2006).

[31] N. Troullier and J. L. Martins, Phys. Rev. B **43**, 1993 (1991).
[32] P. Rivero, V. M. García-Suárez, D. Pereñiguez, K. Utt, Y. Yang, L. Bellaiche, K. Park, J. Ferrer, and S. Barraza-Lopez, Comput. Mater. Sci. **3**, 21 (2015).
[33] P. Hyldgaard, K. Berland, and E. Schröder, Phys. Rev. B **90**, 075148 (2014).
[34] G. Román-Pérez and J. M. Soler, Phys. Rev. Lett. **103**, 096102 (2009).
[35] J. Junquera, O. Paz, D. Sánchez-Portal, and E. Artacho, Phys. Rev. B **64**, 235111 (2001).
[36] H. J. Monkhorst and J. D. Pack, Phys. Rev. B **13**, 5188 (1976).
[37] M. Mehboudi, B. M. Fregoso, Y. Yang, W. Zhu, A. van der Zande, J. Ferrer, L. Bellaiche, P. Kumar, and S. Barraza-Lopez, Phys. Rev. Lett. **117**, 246802 (2016).
[38] See supplementary materials.
[39] S. Liang, H. Yang, P. Renucci, B. Tao, P. Laczkowski, S. Mc-Murtry, G. Wang, X. Marie, J.-M. George,S. Petit-Wetelot, A. Djeffal, S. Mangin, H. Jaffrès, and Y. Lu, Nat. Commun. **8**, 14947 (2017).
[40] W. Han and R. K. Kawakami, Phys. Rev. Lett. **107**, 047207 (2011).